RESEARCH ARTICLE

AuPd bimetallic nanoparticle decorated TiO$_2$ rutile nanorod arrays for enhanced photoelectrochemical water splitting

Roozbeh Siavash Moakhar[1,2,3] · Mahsa Jalali[1,2] · Ajay Kushwaha[2] · Gregory Kia Liang Goh[2] · Nastaran Riahi-Noori[3] · Abolghasem Dolati[1] · Mohammad Ghorbani[1]

Abstract

Here, the synthesis of TiO$_2$ rutile nanorod arrays (TiO$_2$ NRs) decorated with bimetallic gold–palladium cocatalyst nanoparticles (AuPd NPs) is described. The modified photoelectrode was characterized by field-emission scanning electron microscopy, high-resolution transmission electron microscopy, energy-dispersive spectroscopy, X-ray diffraction analysis, X-ray photoelectron spectroscopy, UV–vis spectroscopy, and electrochemical impedance spectroscopy (EIS). AuPd–TiO$_2$ NRs (AuPd–TiO$_2$) demonstrate high photocatalytic activity for photoelectrochemical (PEC) water splitting. The tailored structure of AuPd–TiO$_2$ depicts a boosted photocurrent of 3.36 mA cm^{-2} under AM 1.5 illumination (100 mW cm^{-2}) and efficiency of 2.31% at a low-voltage bias of 0.28 V vs. Ag–AgCl. EIS and Mott–Schottky plots reveal that AuPd–TiO$_2$ has the lowest charge transfer resistance and highest carrier density which suggest a faster carrier transfer. These results indicate that AuPd NPs inherit both properties of light sensitizer from Au and faster electrocatalytic activity of Pd, thus not only generating hot electrons due to the surface plasmonic effect but also facilitating transfer of these electrons to the TiO$_2$ NRs because of high electrocatalytic activity. Moreover, AuPd NPs contribute to the overall enhancement of PEC performance by producing a Schottky barrier, hindering electron–hole recombination and passivating surface defects/traps of TiO$_2$ NRs which eventually enhances the photocurrent significantly.

Graphical Abstract
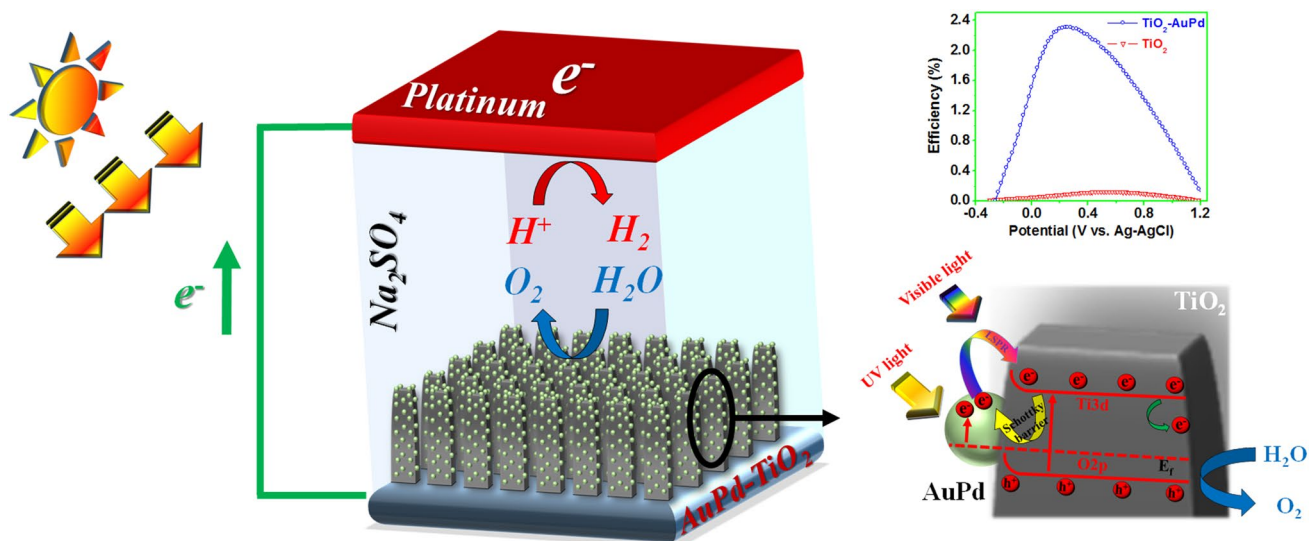
Extended author information available on the last page of the article

1 Introduction

The estate of acquiring sustainable energy sources has been extensively growing in the past decade due to an increasing population, diminution of fossil fuels, increasing awareness of climate change, and global rising living standards [1–3]. Hydrogen is a very noteworthy candidate as a clean fuel because of its high energy density and environmentally friendly chemical byproduct, and can be produced from water and sunlight. Since the breakthrough by Honda and Fujishima [4], extensive efforts have been dedicated to improve photoelectrochemical cell (PEC) water splitting based on titanium dioxide (TiO_2) as a photoanode due to its advantageous band-edge positions, robust optical absorption, non-toxicity, superior photochemical/thermal resistance, and low production cost [5, 6].

The overall TiO_2-based PEC water splitting reaction includes three major steps: (i) light absorption by TiO_2 to produce electron–hole pairs, (ii) charge separation and transfer to the surface, and (iii) surface reactions for water oxidation or reduction [7]. However, TiO_2 suffers from low quantum efficiencies and corresponding rapid electron–hole recombination kinetics as its wide bandgap only allows harvesting the UV spectrum of solar energy. Therefore, extensive efforts have been employed to enhance the light harvesting (step i) and charge separation and migration (step ii). A series of strategies have been applied including elemental doping [8], coupling with dye molecules [9] or using of small-band-gap quantum dots sensitizers [10], surface plasmon effect (SPR) [11, 12], and core–shell nanocomposites [13]. Furthermore, the third step is boosted by the use of a H_2-evolution or O_2-evolution cocatalysts [14, 15]. In photocatalytic water splitting, cocatalysts play three different crucial roles of enhancing the activity and reliability of the semiconductor photocatalyst: (i) decrease the activation energy or overpotential for H_2- or O_2-evolution reactions on the surface of semiconductor, (ii) facilitate electron–hole separation at the cocatalyst/semiconductor interface, and (iii) prevent photocorrosion and elevate the stability of semiconductor photocatalysts.

Currently, most of the developed photocatalyst systems employ noble metal cocatalysts such as Au [15], Ag [16], Pt [17], and Pd [18, 19] to attain high photocatalytic activity. Au is a noble metal which has many benefits including: no corrosion during the photoreaction, and strong interaction with incident light in both visible and infrared regions because of the localized surface plasmon resonance (LSPR) effect [20]. TiO_2 NRs can be sensitized to light with energy below the bandgap by plasmonic Au NPs, which leads to the production of additional charge carriers for water oxidation [21]. Many Au–TiO_2 composite systems have been reported for efficient solar water splitting [22, 23]. Zhang et al. [24] fabricated plasmonic Au nanocrystal-coupled TiO_2 nanotube which exhibited superb PEC water splitting performance with photoconversion efficiency of 1.1%. Moreover, in another research, TiO_2-branched nanorod arrays with plasmonic Au nanoparticles showed the photoconversion efficiency of 1.1% [20]. On the other hand, Pd has a great potential for its unique electronic structure, photocatalytic activity, and thermal properties [25]. In addition, Pd could also effectively hinder the electron–hole recombination at the TiO_2 surface [18]. On the other hand, alloy nanoparticles demonstrate excellent characteristics [26–30]. Consequently, based on this history of applicability of using both Au and Pd NPs in PEC water splitting, we were encouraged to examine AuPd bimetallic alloy nanoparticles. To the best of our knowledge, there is no report of Au–Pd nanoalloy decorated one-dimensional TiO_2 NRs for PEC water splitting.

In the present work, we report the facile and direct surface decoration of TiO_2 nanorods by bimetallic AuPd NPs without using any surfactant or polymer. We found that AuPd bimetallic NP-decorated TiO_2 NR photoelectrodes shows the highest photoconversion efficiency (2.31%) under AM 1.5 irradiation among other decorated TiO_2 1D nanostructures. The mechanism of such an improvement was also deeply discussed. Our results will pave the way for researchers to examine other bimetallic NPs decoration for photoelectrochemical water splitting applications.

2 Experimental

2.1 Growth of TiO_2 NRs on FTO substrate

Twelve milliliters of hydrochloric acid 37% and 12 mL of deionized water were mixed and stirred at ambient conditions for 10 min before the addition in a Teflon-lined stainless-steel autoclave (100 mL total volume, Parr Instrument Co.) at the room temperature. After stirring for another 10 min, one sample of fluorine doped tin oxide (FTO) substrates (F:SnO_2, Tec 15, 15 Ω/sq), ultrasonically cleaned for 60 min in a mixed solution of detergent, deionized water, acetone, and 2-propanol with volume ratios of 1:1:1:1, which were placed at 45° against the wall of the Teflon-liner with the conducting side facing down. The hydrothermal synthesis was conducted at 150 °C for 2–4 h in an oven. After synthesis, the autoclave was cooled to room temperature in air for 30 min. The FTO substrate was taken out, rinsed with deionized water, and dried with N_2.

2.2 Photoanode preparation

Cyclic voltammetry (CV) technique was utilized to decorate TiO_2 NRs with Au, Pd, and Au–Pd cocatalyst NPs at a scan rate of 20 mV s^{-1} for one cycle at the room temperature. All CVs were performed using Autolab 302N potentiostat/galvanostat equipped with FRA32M and controlled by the Nova 1.10 software in a setup of three-electrode cell. FTO/TiO_2 electrode was used as a working electrode. The saturated calomel electrode (Ag–AgCl) served as the reference electrode, and a platinum wire as a counter electrode. The conducting area of each electrode was restricted to 1×1 cm^2 by wrapping them with Teflon tape. 0.75 mM $HAuCl_4$ (Sigma-Aldrich) and 0.25 mM H_2PdCl_4 (Sigma-Aldrich) were used in 0.1 M KCl (Sigma-Aldrich) solutions for electrodeposition of AuPd NPs in addition to pure Au (1 mM $HAuCl_4$) and Pd (1 mM H_2PdCl_4). All aqueous solutions were prepared with Millipore water (Milli-Q).

2.3 Morphological and structural characterizations

Field-emission scanning electron microscopy analysis was performed using an FESEM JEOL JSM7600F to investigate the surface morphology as well as elemental composition. High-resolution TEM (HRTEM) images and energy-dispersive spectroscopy (EDS) were obtained with a JEOL 2100 HRTEM at an accelerating voltage of 200 kV. The identification and purity of the phase was evaluated by an X'Pert Pro MPD (PANalytical) unit. X-ray photoelectron spectroscopy (XPS) experiments were performed using ESCA Lab 250i-XL. Furthermore, no internal standard was used for the calibration of the instrument and to further discuss the attribution of XPS signals.

2.4 Photoelectrochemical characterization

Three-electrode based photoelectrochemical measurements were performed using Autolab potentiostat/galvanostat 302N. AuPd NPs' decorated TiO_2 NRs films were used as working electrode (photoanode), Pt wire as counter, and Ag–AgCl as reference electrode in 0.1 M Na_2SO_4 electrolyte solution. The photoanodes were illuminated by Xenon lamp using a solar simulator under 1.5 AM (100 mW cm^{-2}) irradiation at 1 cm^2 area for photoelectrical measurements. Photocurrent measurements were performed at $+400$ mV fixed bias with respect to Ag–AgCl reference electrode. Linear sweep voltammetry measurements were performed in the potential range of -0.4 to 1.2 V vs. Ag–AgCl at a scan rate of 50 mV s^{-1}. Three different electrodes named as Au–TiO_2 (TiO_2 NRs decorated with Au NPs), Pd–TiO_2 (TiO_2 NRs decorated with Pd NPs), and AuPd–TiO_2 (TiO_2 NRs decorated with AuPd NPs) were tested for PEC measurements. Electrochemical impedance spectroscopy (EIS)

was performed in a 0.1 M Na_2SO_4 aqueous solution at open circuit potential and 10 mV amplitude over the frequency range of 10^5–0.001 Hz.

3 Results and discussion

3.1 Morphological and structural properties

Figure 1 presents the typical top-view SEM micrograph of bare and bimetallic Au–Pd NPs decorated TiO_2 NRs.

The SEM images in Fig. 1 a, b show highly ordered, compact, one-dimensional architecture of the TiO_2 NRs. The NRs possess average diameter and length of 150–200 nm and 2.8 μm, respectively. Figure 1 c, d depicts the SEM images of AuPd–TiO_2 NRs. No obvious changes in morphology can be observed in comparison with pristine TiO_2. The AuPd NPs are directly deposited on the TiO_2 NR surface without any intermediate surface ligands/binders which makes it more favorable for photocatalytic activity.

To attain more detailed structural information, the rutile TiO_2 NRs and AuPd NP-decorated TiO_2 NRs were further investigated by HRTEM, as shown in Fig. 2a, b, respectively. The crystallinity of TiO_2 NRs was clearly evidenced by clearly visible lattice fringes in higher resolution TEM imaging (inset of Fig. 2a). D-spacing value for lattice planes of TiO_2 nanostructures was 3.2 and 2.9 Å for (110) and (001), respectively which are in good agreement with the rutile phase TiO_2 [31]. HRTEM image (Fig. 2b) showed the AuPd NPs supported on TiO_2 NRs. Furthermore, inset of Fig. 2b demonstrates the EDS results recorded on an individual AuPd NPs decorated TiO_2 NRs, which confirmed the presence of AuPd NPs.

The absence of any other elemental peaks confirmed that the AuPd NP decoration of TiO_2 NRs via electrodeposition with no reducing or stabilizing agents is a clean process, which result in no contamination issues from hydrocarbons which is typically a big concern during sol–gel processing. The EDS mapping of an NR confirms the uniform distribution of AuPd NPs, as well as their alloy nature (Fig. 2c–g).

Figure 3a shows the X-ray diffractogram of the bare TiO_2 and surface modified TiO_2 NR films. All the diffraction peaks agree well with the tetragonal rutile phase [32] of TiO_2. The peaks at 44.5°, 40.2°, and 46.7° are attributed to the Au(200), Pd(111), and Pd(200) (Fig. 3b). Two additional peaks can be seen at 38.7° and 44.8° of 2θ in the AuPd–TiO_2, which might be due to the presence of the bimetallic AuPd NPs. The broad peak at 38.7° is located between the Au(111) [33] and Pd(111) [34], whilst the diffraction peak at 44.9° is between the Au(200) and Pd(200). Vegard's law was used to determine the bulk composition of AuPd–TiO_2 photoelectrode, which was 0.74:0.26 of Au:Pd.

Fig. 1 Top-view SEM micrograph of bare TiO_2 NRs: **a** lower magnification (the inset is cross-sectional view), **b** higher magnification (the inset is single TiO_2 NR), AuPd–TiO_2, **c** lower magnification (the inset is cross-sectional view), and **d** higher magnification (the inset is single AuPd–TiO_2 NR)
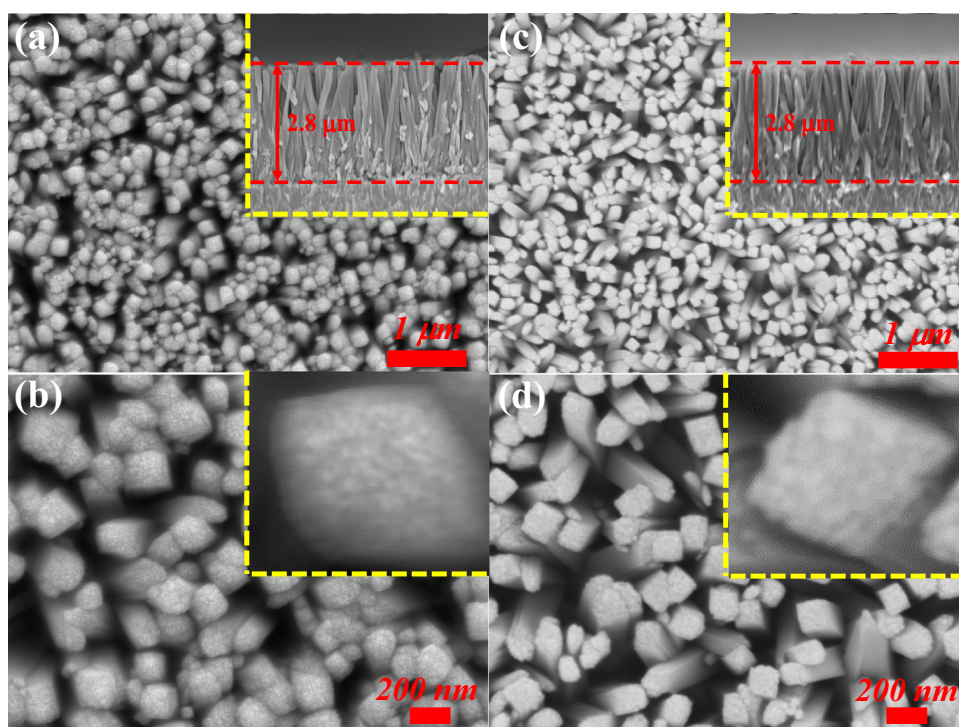
XPS was employed to analyze the specific surface composition of the samples (Fig. 4). From Fig. 4a, two peaks at 458.94 and 464.82 eV correlate to $Ti2p_{3/2}$ and $Ti2p_{1/2}$, and correspond to the spin–orbit components of Ti^{4+} state of oxidation and represent the oxide phase of titanium [20]. However, a small shift of 0.19 eV is observed from TiO_2 (458.94 eV) to TiO_2/AuPd (459.13 eV), which indicates the electron transfer between the NPs and TiO_2 [35]. In O_{1s} spectra (Fig. 4b), a sharp peak at 530.18 eV and a broad one at 531.79 eV are observed, which corresponds to O^{2-} in the TiO_2 lattice and Ti–OH, respectively [36]. Consequently, from these results, it could be determined that the chemical states of Ti and O in the TiO_2 matrix were not affected by introducing AuPd NPs.

As shown in Fig. 4c, two peaks at 83.47 and 87.15 eV correspond to $Au4f_{7/2}$ and $Au4f_{5/2}$ which reveal the Au^0 oxidation state [37]. Similarly, in Fig. 4d, two peaks at 334.99 and 340.25 eV correspond to $Pd3d_{5/2}$ and $Pd3d_{3/2}$ which correlate to Pd^0 oxidation state [38], serving as proof of the metallic states of Au and Pd. Noteworthy, both $Au4f_{7/2}$ and $Pd3d_{5/2}$ show relative negative shift of 0.30 and 0.15 eV in comparison to Au–TiO_2 ($4f_{7/2}$ at 83.77 eV) and Pd/TiO_2 ($3d_{5/2}$ at 335.13 eV), respectively. This lower binding energy might be caused by the electron transfer from oxygen vacancies of TiO_2 to the bimetallic AuPd NPs [39].

In addition, both Au (Fig. 4e) and Pd (Fig. 4f) monometallic NPs also show negative shifts of 0.23 and 0.27 eV compared with metallic Au ($4f_{7/2}$ at 84 eV) and Pd ($3d_{5/2}$ at 335.4 eV), respectively. The negative shift which occurs

for both bimetallic and monometallic NPs suggests strong interaction between these nanoparticles and the TiO_2 NRs [40]. Moreover, since Au and Pd have lower Fermi level than TiO_2, once they are electrically connected, an upward energy band bending is expected and a Schottky contact will be formed at the interface region, and therefore, electrons will readily migrate from the semiconductor to the bimetallic nanoparticles (Scheme 1). As a result, the surface of the AuPd clusters supported on TiO_2 NRs attains an excess of negative charges [40]. From XPS, the ratio of Au:Pd obtained 2.92:1 indicates that the Au–Pd NPs composition is similar to the electrolyte composition.

Figure 5 shows the UV–visible spectrum of bare TiO_2 NRs as well as TiO_2 NRs modified with Pd NPs, Au NPs, and AuPd NPs, respectively. The Au–TiO_2 NRs show strong absorption of visible light at about 540 nm, mainly because of the LSPR effect of the Au nanoparticles. However, the AuPd–TiO_2 exhibits the highest absorption with a broad plasmon band with the maximum at around 540 nm. A broad plasmon band was also observed in bimetallic AuAg alloy NPs [41, 42], which can confirm formation of alloy NPs, as well.

3.2 Photoelectrochemical measurement

Figure 6a shows the time-dependent photocurrent measurements of bare TiO_2 and TiO_2 decorated with AuNPs, Pd NPs, and AuPd NPs' anodes, respectively, and current densities achieved under ON/OFF conditions at a fixed 0.4 V
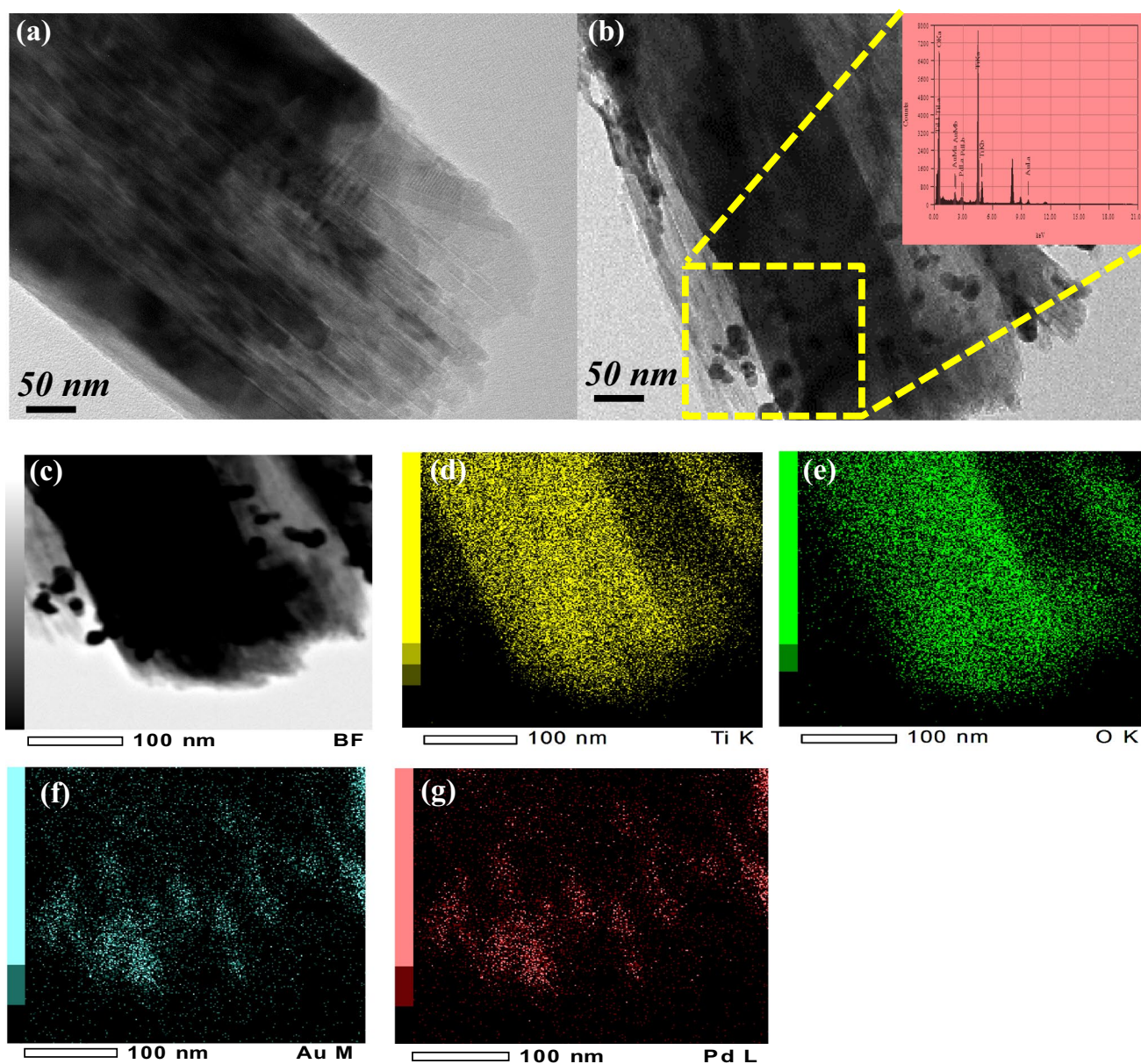
Fig. 2 TEM images of **a** TiO$_2$ (the inset is HRTEM image of TiO$_2$) and **b** AuPd–TiO$_2$ (the inset is EDS result); EDS elemental mapping of AuPd–TiO$_2$: **c** TEM image; **d–g** corresponding elemental mapping of Ti, O, Au, and Pd, respectively

vs. Ag–AgCl external bias. AuPd–TiO$_2$ shows a drastically higher value of photocurrent in comparison with other photoanodes. The increment in photocurrent correlates to the presence of metallic and bimetallic NPs over the surface of TiO$_2$ nanorods, which enhances the charge separation process, and leads to the increases in the photocurrent density. Furthermore, bimetallic NPs as a novel brand of semiconductor–metal system can extensively improve photoelectron generation efficiency due to combination of their parties properties and synergic effect of counterparts [26, 43]. Moreover, high surface energy and the different electronic structures of bimetallic NPs from their pure state [44] lead

to their excellent electrocatalytic properties. The synergy of bimetallic noble metals and semiconductor photocatalysts brings in noteworthy changes to many aspects of photocatalysis. Figure 6b illustrates the stability of AuPd–TiO$_2$ NRs photoresponse over a long period of time. As it can be observed, photocurrent is almost steady with minimum variation/fluctuation for 3 h continuous measurement.

Figure 6c illustrates the photoelectrochemical properties of TiO$_2$ NR-based photoanodes. The photocurrent measured under illumination is a direct reflection of the water splitting rate and reveals the number of charge carriers generated from the incident light which, subsequently, will contribute

Fig. 3 **a** XRD analysis of FTO, TiO_2, Pd–TiO_2, Au–TiO_2, and AuPd–TiO_2; **b** short range XRD pattern of decorated TiO_2 NRs as indicated
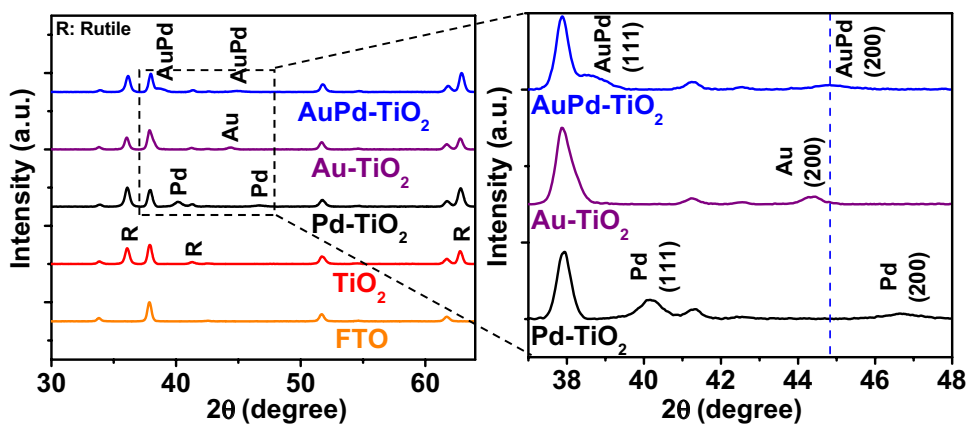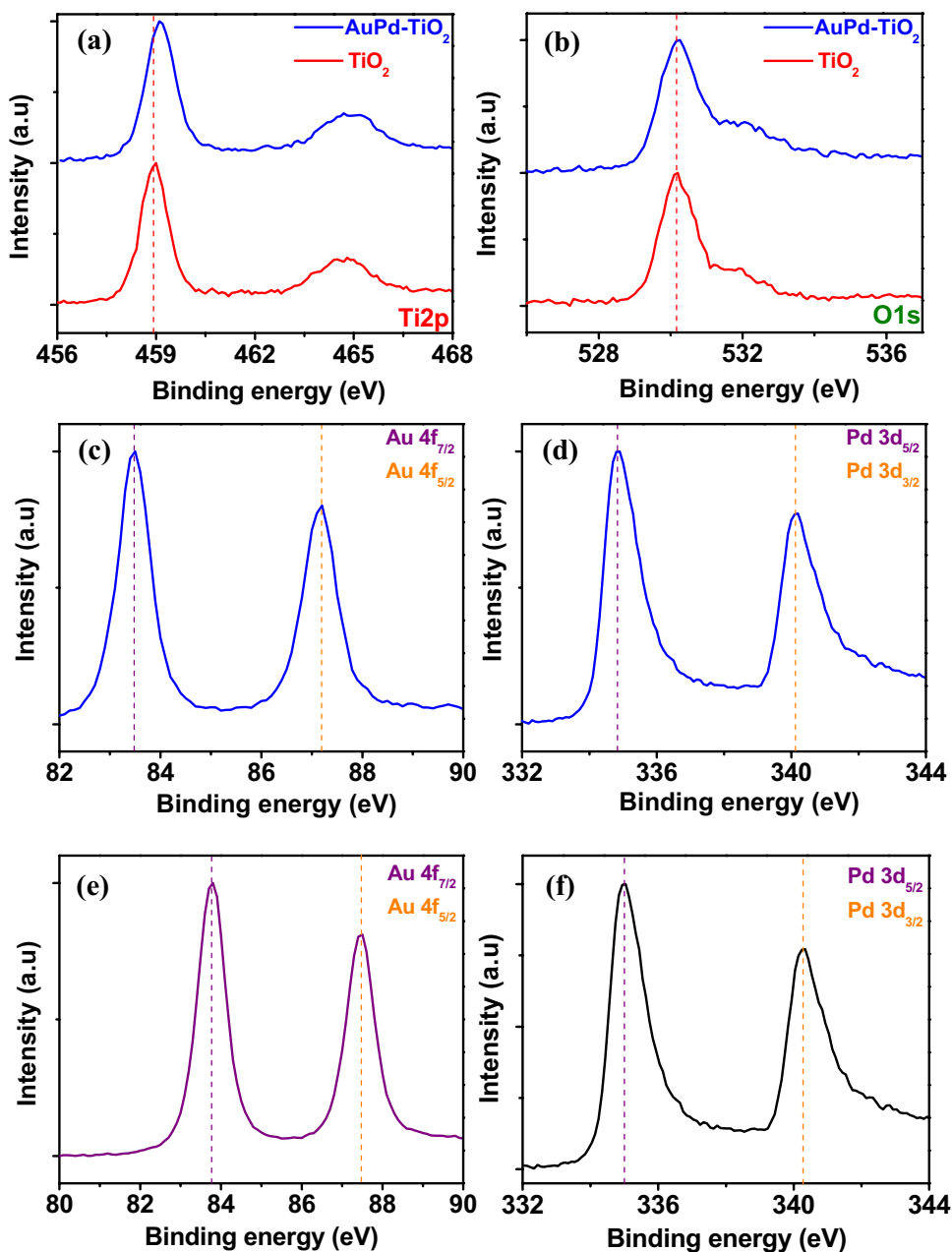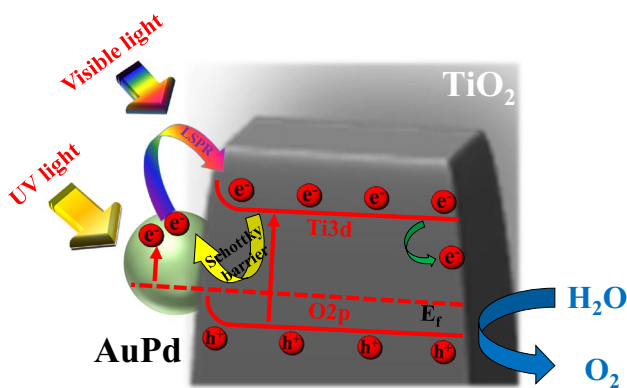

Fig. 4 **a** Ti2p and **b** O1s XPS spectra of TiO_2 and AuPd–TiO_2; **c** Au4f and **d** Pd3d XPS spectra of AuPd–TiO_2; **e** Au4f and **f** Pd3d XPS spectra of Au–TiO_2 and Pd–TiO_2, respectively

Scheme 1 Schematic diagram illustrating the photoelectrochemical water splitting process over AuPd–TiO$_2$ under sun simulator irradiation
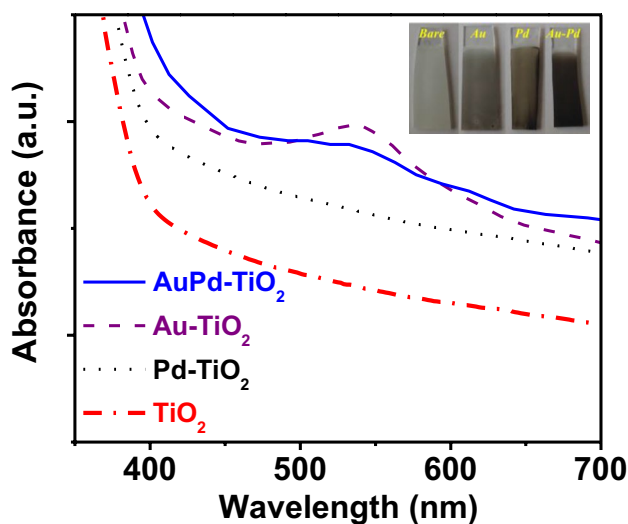

Fig. 5 UV–vis absorption spectra of TiO$_2$, Pd–TiO$_2$, Au–TiO$_2$, and AuPd–TiO$_2$

in the water oxidation reaction on the photoanode and hydrogen ion reduction on the counter electrode. The bare TiO$_2$ photoanode has the lowest value (0.26 mA cm^{-2} at 1 V vs. Ag–AgCl) mainly due to high recombination. Among decorated samples, the AuPd–TiO$_2$ photoanode shows the highest value of photocurrent density, indicating its highest photoelectrocatalytic activity. Furthermore, Au NP- and Pd NP-decorated TiO$_2$ photoanodes have lower photocurrent values.

As it can be observed, the obtained current density from Fig. 6a is much lower than that in Fig. 6c at an applied potential of +0.4 V. To clarify the reason behind this phenomenon, it should be noted that, in chronoamperometry (Fig. 6a), potential is kept at a constant value and current is measured as a function of time, whilst, in CV (Fig. 6c), the potential is swept from −0.4 to 1.2 V vs. Ag/AgCl. Therefore, the current density obtained from Fig. 6a is the

steady-state value and that represents the catalytic interface property on overpotential at a defined current density merely derived from faradaic reaction. Nevertheless, the current density obtained from Fig. 6c is a potentiodynamic method in which the current arises from both faradaic and nonfaradic processes on polarized interface at an unequilibrated state.

A similar relationship between the loading amount of cocatalyst and the photocalytic activity was observed irregardless of whether a mono or bimetallic NP cocatalyst was employed (Fig. 7a). Their associate microstructures are also shown in Fig. 7b. As it can be observed, loading of bimetallic NP is increased by ascending the cycle from 0.5 to 8. At the initial stage, increasing loading of cocatalyst steadily enhances the TiO$_2$ NR water splitting activity by facilitating charge collection and the surface plasmonic effect (0.5 and 1 cycles). At the optimal loading value of coctalyst (1 cycle), the highest photocatalytic activity is achieved. Ultimately, further loading of the cocatalyst (2, 4 and 8 cycles) will drastically decrease the photocatalytic activity due to several reasons: (i) screening of the surface-active sites of the TiO$_2$ NRs from contact with water molecules, (ii) obstruction of incident light, and hence inhibiting the light absorption and photogeneration electrons and holes inside the TiO$_2$ NRs, (iii) acting as charge recombination centers, leading to the decrease of the photocatalytic activity.

The efficiency calculation is a thermodynamically related measure of the efficiency of the instantaneous conversion of free energy by the device. The inherent assumption involved in this method is that the energy stored in the photoelectrolysis products can be recovered in a hypothetical ideal fuel cell. The efficiencies of solar-driven hydrogen generation of all four photoanodes are calculated using Formula 1 and listed in Table 1 [45]:

$$\eta(\%) = \frac{J_P(1.23 - V)}{L_{light}} \times 100, \tag{1}$$

where J_P (mA cm^{-2}) corresponds to current density, V (volt) is applied voltage, and L_{light} (mW cm^{-2}) represents the incident light power.

The lowest efficiency is related to as-prepared TiO$_2$, and relatively, Pd-, Au-, and AuPd-decorated TiO$_2$ photoanodes have higher efficiency (Fig. 6d). Moreover, the average yield of photoconversion (obtained from five devices) of TiO$_2$, Pd–TiO$_2$, Au–TiO$_2$, and AuPd–TiO$_2$ is 0.11, 0.98, 1.49, and 2.28%, respectively. A significant increment in efficiency is seen for the AuPd-decorated TiO$_2$ photoanode. This photoanode can absorb visible light in a wide wavelength range (broad LSPR peak) which leads to the utilization of a large amount of incident photons and, thus, cause less saturated photogenerated electrons, fast electron transfer, and hindered recombination process [46]. The photogenerated electrons from separated electron–hole

Fig. 6 **a** Time-dependent photoresponse of TiO_2, Pd–TiO_2, Au–TiO_2, and AuPd–TiO_2 at an applied potential of +0.4 V vs. Ag/AgCl under the sun simulator illumination; **b** photocurrent of AuPd–TiO_2 during 3 h; **c** I–V curves of TiO_2, Pd–TiO_2, Au–TiO_2, and AuPd–TiO_2 under dark and light conditions; **d** photoconversion efficiency as a function of the applied potential
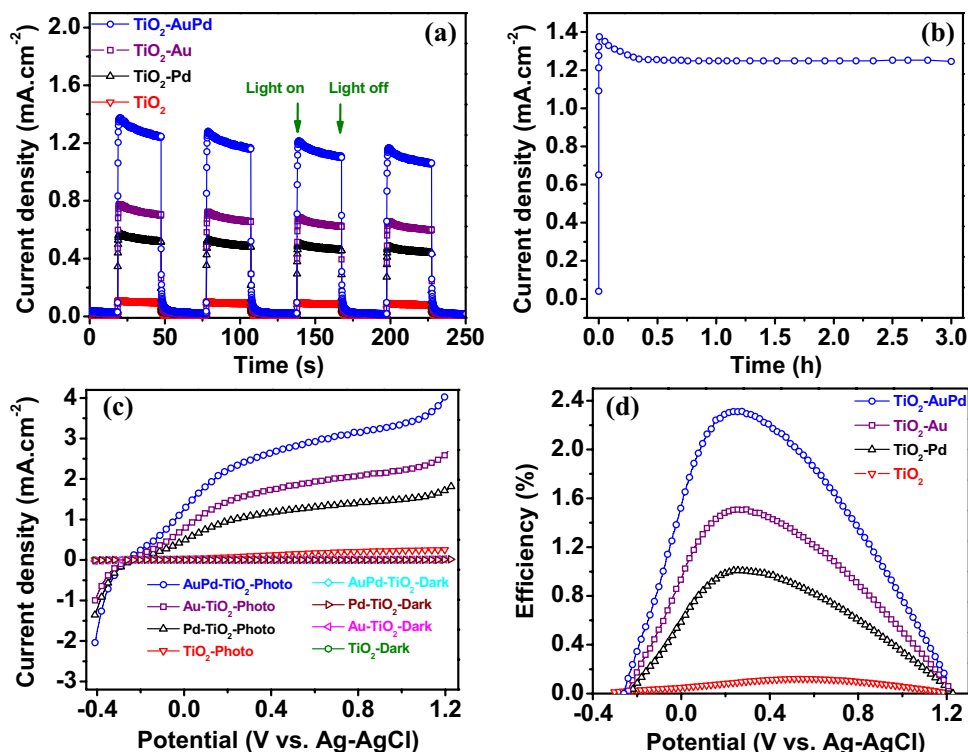
pairs migrate along the nanorods to form OH^- and H^+ radicals in solution, which leads to generation of H_2 on Pt electrode. Furthermore, Pd serves as a promoter to offer reactive oxygen in oxidation reactions in addition to facilitate electron–hole separation and promotes interfacial electrons transfer.

Comparing photoconversion efficiency with other noble metal decorated photoelectrode system, our bimetallic AuPd–TiO_2 NRs photoelectrode exhibits significantly higher value (2.31%) than that of Au–TiO_2 nanotube (1.1%) [24] and Au–TiO_2-branched NR arrays' (1.27%) [20] photoelectrodes under similar conditions.

To clarify the origin of the photocurrent improvement of decorated TiO_2 photoanode, IV curves in dark have been studied (Fig. 7c). As can be observed, bare TiO_2 NRs show the lowest photocurrent, confirming its low photoelectrocatalytic activity [47]. Interestingly, Pd–TiO_2 NRs shows higher injection currents compared with Au–TiO_2 NRs. This demonstrates that Pd NPs have higher ability on the charge transfer between TiO_2 and the aqueous solution than Au NPs, which is in agreement with the EIS results under dark condition (Fig. 8a, where Pd–TiO_2 shows lower charge transfer resistance). Under the same illumination condition, TiO_2 NRs decorated with bimetallic cocatalysts exhibits a higher current in regard to monometallic ones [48]. Moreover, a characteristic oxidation peak at −0.15 V vs. Ag–AgCl is detected for all decorated samples. Since no such a peak is observed for bare TiO_2 NRs in the available oxidation

window, this peak could be related to the electrochemical generation of holes on noble nanoparticles [49].

Further studies have been performed by placing 495 nm cut-off filter between the light source and the sample with the purpose of excluding the TiO_2 contribution to the photoresponse (Fig. 7d). The results indicate that no photocurrent is generated when using bare TiO_2 NRs, while, in contrast, the presence of noble nanoparticles introduces visible light photoactivity. Interestingly, comparing Au and Pd monometallic decorated TiO_2 NRs shows that Au–TiO_2 NRs have higher photocurrents attributed to its surface plasmon resonance effect [15]. AuPd–TiO_2 has higher photocurrent in comparison with monometallic decorated TiO_2 NRs. Herein, electron–hole pairs are generated near the TiO_2 NRs surface due to the interaction of localized electric field of AuPd NPs with TiO_2 surface [46]. AuPd has less unfilled d states as a result of electron transfer from Pd to 5d Au orbits [50] leading to electron-rich Au sites. These electrons of AuPd are in higher energetic state [51] and, thus, could be easily transferred to the TiO_2 conduction band generating an improved photocurrent. Likewise under dark condition, characteristic oxidation peak at around −0.15 V vs. Ag–AgCl is also detected for all decorated samples.

3.3 EIS characterization

The EIS is a powerful tool for studying the interfacial properties at the electrodes and solutions. Figure 8a, b shows the
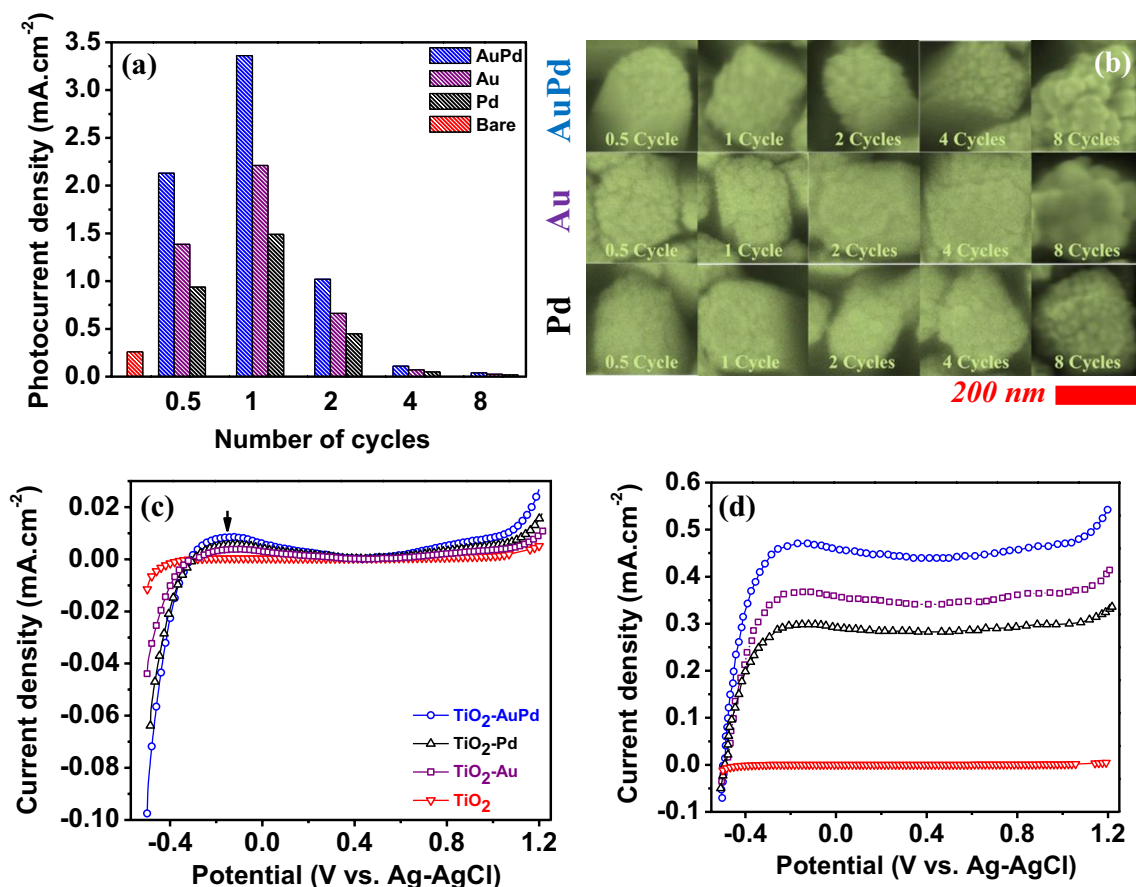
Fig. 7 **a** Photocurrent density of TiO_2, Pd–TiO_2, Au–TiO_2, and $AuPd$–TiO_2 decorated for 0.5, 1, 2, 4, and 8 cycles, and **b** their corresponding SEM images; I–V curves of TiO_2, Pd–TiO_2, Au–TiO_2, and $AuPd$–TiO_2 under **c** dark and **d** visible light conditions

**Table 1** Summary of photoelectrochemical properties of TiO_2, Pd–TiO_2, Au–TiO_2, and $AuPd$–TiO_2

Sample	J at 1 V vs. Ag–AgCl (mA cm^{-2})	Efficiency (%)	J @ max efficiency (mA cm^{-2})	R_{ct}-dark (MΩ)	R_{ct}-photo (kΩ)	N_D ($\times 10^{18}$)	U_{FB} (V vs. Ag–AgCl)	k_{app} (cm s^{-1})
TiO_2	0.26	0.12	0.17	2.1	70.6	1.88	−0.758	3.72×10^{-8}
Pd–TiO_2	1.49	1.01	1.04	1.3	39.6	7.28	−0.661	6.63×10^{-8}
Au–TiO_2	2.21	1.51	1.53	1.9	30.4	12.60	−0.755	8.64×10^{-8}
$AuPd$–TiO_2	3.36	2.31	2.44	1.2	19.3	79.00	−0.500	1.36×10^{-7}

Nyquist plots at open circuit potential for bare TiO_2NRs and Pd NP-, Au NP-, and AuPd NP-decorated TiO_2 NR photoanodes in 0.1 M Na_2SO_4, in the dark and under illumination, respectively. Figure 8c shows the equivalent circuit used to fit experimental data of the Nyquist plots. In this model, the resistance between the space charge layer and open Helmholtz layer was deliberated reliant on the double layer capacitance (C_{dl}) and charge transfer resistance (R_{ct}) [52].

The impedance spectra composed of a semi-circle segment which correlates to the electron-transfer process. Thus, classical Randles circuit can be employed to describe the interface [53]. R_s represents the resistance of electrolyte solution, C_{dl} indicates the interface capacitance of electrode and electrolyte, and in the interim, R_{ct} depicts charge transfer resistance. Their corresponding values are summarized in Table 1. As can be observed, bimetallic AuPd NPs drastically decrease the charge transfer resistance. This lower charge transfer leads to higher photoelectrocatalytic activity [6]. In addition, comparing Fig. 8a, b clearly reveals that, for all samples, R_{ct} under illumination is much smaller than that in the dark, indicating
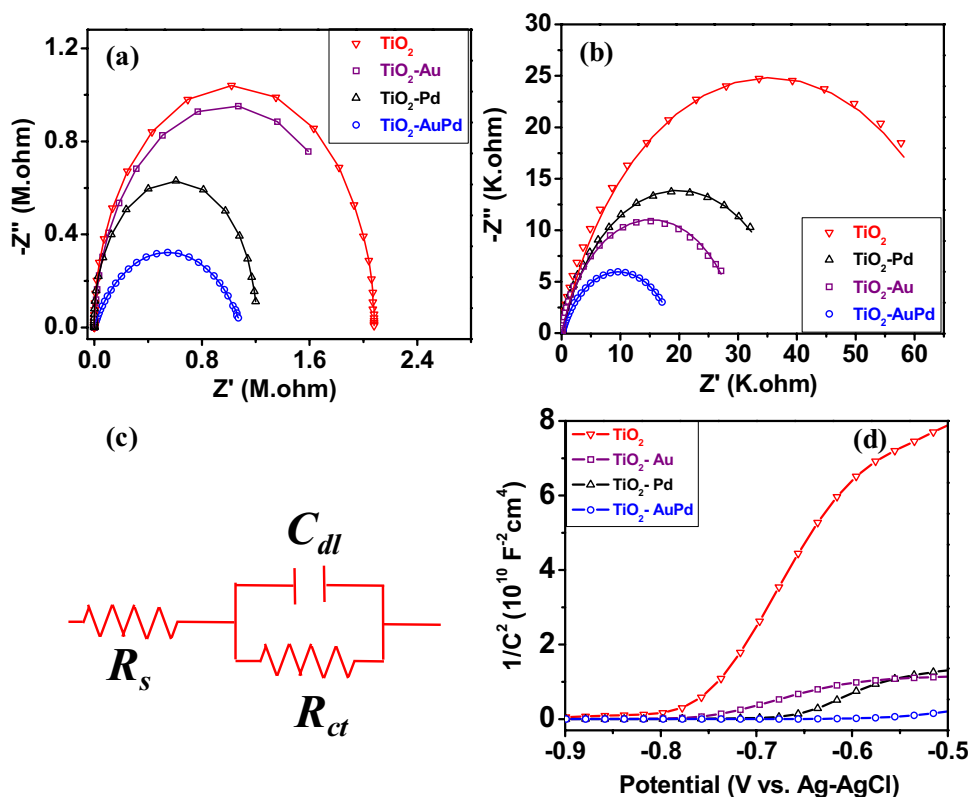
that photoinduced electrons are involved in the electron transfer across the photoelectrode/solution interface [54].

The Mott–Schottky (MS) plot (Fig. 8d) was conducted from the electrochemical impedance measurement at 0.5 kHz to determine the flat band potential (U_{FB}) and carrier density (N_D) following the Formula 2 [18]:

$$\frac{1}{C^2} = \frac{2}{N_D e \varepsilon_0 \varepsilon}\left[(U_s - U_{FB}) - \frac{kT}{e}\right], \tag{2}$$

where C is the space charge capacitance in the semiconductor; N_D is the electron carrier density; e is the elemental charge value; ε_0 is the permittivity of the vacuum; ε is the relative permittivity of the semiconductor; U_s is the applied potential; T is temperature; k is the Boltzmann constant. As depicted in Fig. 8d, all the four samples have a positive slope, indicating n-type semiconductors. The flat band potential (U_{FB}) value can be estimated by extrapolating the MS plots to the potential axis (i.e., $1/C^2 = 0$) to get the intercept. From Fig. 8d, the carrier density N_D can also be calculated, from Formula 3 [18]:

$$N_D = -\left(\frac{2}{e\varepsilon_0\varepsilon}\right)\left(\frac{d(U_s)}{d(1/C^2)}\right). \tag{3}$$

For rutile TiO$_2$ ($\varepsilon = 170$) [55], the U_{FB} and N_D values are calculated and summarized in Table 1. The positive shift of

U_{FB} for AuPd–TiO$_2$ relative to the other samples indicates a decrease in bending band edge which leads to assist the electron transfer [56]. Moreover, the higher N_D of AuPd–TiO$_2$ also suggested a faster carrier transfer than the other samples, and thus lead to an improvement in PEC performance [20].

Formula 4 was applied to calculate the apparent electron-transfer rate constant (k_{app}) and the results are summarized in Table 1:

$$k_{app} = \frac{RT}{F^2 R_{ct} A C}, \tag{4}$$

where R is the universal gas constant, T is the temperature (298 K), F is the Faraday constant, R_{ct} is the resistance to charge transfer under illumination, A is the surface area of the electrode, and C is the concentration of Na$_2$SO$_4$ (100 mM). The k_{app} also confirms that the photoelectron transfer is fastest on AuPd–TiO$_2$ than the rest of the photoelectrodes.

As a result, based on these studies, the mechanism of AuPd–TiO$_2$ PEC enhancement under sun simulator irradiation can be discussed as follows and a schematic diagram is presented in Scheme 1. Under visible region of incident light, AuPd NPs can dramatically increase the light absorption and inject hot electrons due to LSPR excitation in a wide-frequency range, and these electrons could be transferred rapidly to the semiconductor. Under UV region of

incident light, AuPd NPs can act as a reservoir for photogenerated electrons [57], which are rapidly transferred from the conduction band of TiO_2 NRs to the AuPd NPs (forming Schottky barrier). The storage of electrons in AuPd NPs reduces charge recombination and leads to improvement of the photoelectrocatalytic activity. All in all, although LSPR still plays an important role, the catalytic effects of bimetallic AuPd BNPs of reducing electron–hole recombination and facilitating charge transfer rate play a more dominant role. This is consistent with Haro et al.'s [58] findings which ascertain that the improvement of the photocurrent due to the presence of plasmonic nanoparticles is mainly related to a catalytic effect, rather than the LSPR effect.

4 Conclusion

In conclusion, vertically aligned TiO_2 rutile NR arrays decorated with AuPd bimetallic NPs cocatalyst were successfully fabricated. The proposed AuPd–TiO_2 photoelectrode demonstrates photocurrent and water splitting efficiency of nearly 13 and 19 times higher than that of the pristine TiO_2 NRs, respectively. The enhanced photoelectrochemical performance could be accredited to photoanode improvements using 'multifunctional' cocatalyst bimetallic nanoparticles. AuPd NPs boost the visible light absorption and produce hot electrons near TiO_2 NRs surface by LSPR excitation which can be transferred quickly thanks to low charge resistance. Our proposed photoelectrocatalyst is highly efficient, eco-friendly, and reusable without producing toxic by-products. Thus, our research opens up a new class of cocatalyst nanostructure that can be used successfully to photoelectrochemical water splitting.

References

1. Cook TR, Dogutan DK, Reece SY et al (2010) Solar energy supply and storage for the legacy and nonlegacy worlds. Chem Rev 110:6474–6502. https://doi.org/10.1021/cr100246c
2. Masudy-Panah S, Moakhar RS, Chua CS et al (2016) Rapid thermal annealing assisted stability and efficiency enhancement in a sputter deposited CuO photocathode. RSC Adv 6:29383–29390. https://doi.org/10.1039/C6RA03383K
3. Arani HF, Mirhabibi A (2016) Effect of nano carbon additives on the microstructure of polyvinyl chloride heated up to 2000 °C. Fullerenes Nanotubes Carbon Nanostruct 24:34–42. https://doi.org/10.1080/1536383X.2015.1110696
4. Fujishima A, Honda K (1972) Electrochemical photolysis of water at a semiconductor electrode. Nature 238:37–38. https://doi.org/10.1038/238037a0
5. Siavash Moakhar R, Masudy-Panah S, Jalali M et al (2016) Sunlight driven photoelectrochemical light-to-electricity conversion of screen-printed surface nanostructured TiO_2 decorated with plasmonic Au nanoparticles. Electrochim Acta 219:386–393. https://doi.org/10.1016/j.electacta.2016.10.022
6. Jalali M, Moakhar RS, Kushwaha A et al (2015) TiO_2 surface nanostructuring for improved dye loading and light scattering in double-layered screen-printed dye-sensitized solar cells. J Appl Electrochem 45:831–838. https://doi.org/10.1007/s10800-015-0852-x
7. Yang J, Wang D, Han H, Li C (2013) Roles of cocatalysts in photocatalysis and photoelectrocatalysis. Acc Chem Res 46:1900–1909. https://doi.org/10.1021/ar300227e
8. Park JH, Kim S, Bard AJ (2006) Novel carbon-doped TiO_2 nanotube arrays with high aspect ratios for efficient solar water splitting. Nano Lett 6:24–28. https://doi.org/10.1021/nl051807y
9. Jalali M, Siavash Moakhar R, Kushwaha A et al (2015) Enhanced dye loading-light harvesting TiO_2 photoanode with screen printed nanorod-nanoparticles assembly for highly efficient solar cell. Electrochim Acta 169:395–401. https://doi.org/10.1016/j.electacta.2015.04.077
10. Wang G, Yang X, Qian F et al (2010) Double-sided CdS and CdSe quantum dot co-sensitized ZnO nanowire arrays for photoelectrochemical hydrogen generation. Nano Lett 10:1088–1092. https://doi.org/10.1021/nl100250z
11. Siavash Moakhar R, Goh GKL, Dolati A, Ghorbani M (2017) Sunlight-driven photoelectrochemical sensor for direct determination of hexavalent chromium based on Au decorated rutile TiO_2 nanorods. Appl Catal B 201:411–418. https://doi.org/10.1016/j.apcatb.2016.08.026
12. Siavash Moakhar R, Goh GKL, Dolati A, Ghorbani M (2015) A novel screen-printed TiO_2 photoelectrochemical sensor for direct determination and reduction of hexavalent chromium. Electrochem Commun 61:110–113. https://doi.org/10.1016/j.elecom.2015.10.011
13. Zhang N, Liu S, Fu X, Xu YJ (2011) Synthesis of M@TiO_2 (M = Au, Pd, Pt) core-shell nanocomposites with tunable photoreactivity. J Phys Chem C 115:9136–9145. https://doi.org/10.1021/jp2009989
14. Ran J, Zhang J, Yu J et al (2014) Earth-abundant cocatalysts for semiconductor-based photocatalytic water splitting. Chem Soc Rev 43:7787–7812. https://doi.org/10.1039/c3cs60425j
15. Pu YC, Wang G, Chang K, Der et al (2013) Au nanostructure-decorated TiO_2 nanowires exhibiting photoactivity across entire UV-visible region for photoelectrochemical water splitting. Nano Lett 13:3817–3823. https://doi.org/10.1021/nl4018385
16. Takai A, Kamat PV (2011) Capture, store, and discharge. Shuttling photogenerated electrons across TiO_2-silver interface. ACS Nano 5:7369–7376. https://doi.org/10.1021/nn202294b
17. Amirav L, Alivisatos AP (2010) Photocatalytic hydrogen production with tunable nanorod heterostructures. J Phys Chem Lett 1:1051–1054. https://doi.org/10.1021/jz100075c
18. Zhang Z, Yu Y, Wang P (2012) Hierarchical top-porous/bottom-tubular TiO_2 nanostructures decorated with Pd nanoparticles for efficient photoelectrocatalytic decomposition of synergistic pollutants. ACS Appl Mater Interfaces 4:990–996. https://doi.org/10.1021/am201630s
19. Moakhar RS, Kushwaha A, Jalali M et al (2016) Enhancement in solar driven water splitting by Au–Pd nanoparticle decoration of electrochemically grown ZnO nanorods. J Appl Electrochem 46:819–827. https://doi.org/10.1007/s10800-016-0981-x
20. Su F, Wang T, Lv R et al (2013) Dendritic Au/TiO_2 nanorod arrays for visible-light driven photoelectrochemical water splitting. Nanoscale 5:9001–9009. https://doi.org/10.1039/c3nr02766j
21. Zhou X, Liu G, Yu J, Fan W (2012) Surface plasmon resonance-mediated photocatalysis by noble metal-based composites under visible light. J Mater Chem 22:21337. https://doi.org/10.1039/c2jm31902k

22. Lee J, Mubeen S, Ji X et al (2012) Plasmonic photoanodes for solar water splitting with visible light. Nano Lett 12:5014–5019

23. Pu YC, Chen YC, Hsu YJ (2010) Au-decorated $NaxH_2-xTi_3O_7$ nanobelts exhibiting remarkable photocatalytic properties under visible-light illumination. Appl Catal B 97:389–397

24. Zhang Z, Zhang L, Hedhili MN et al (2013) Plasmonic gold nanocrystals coupled with photonic crystal seamlessly on TiO_2 nanotube photoelectrodes for efficient visible light photoelectrochemical water splitting. Nano Lett. https://doi.org/10.1021/Nl3029202

25. Wang Y, Chu W, Wang S et al (2014) Simple synthesis and photoelectrochemical characterizations of polythiophene/Pd /TiO_2 composite microspheres. ACS Appl Mater Interfaces 6:20197–20204

26. Panigrahy B, Sarma DD (2014) Enhanced photocatalytic efficiency of AuPd nanoalloy decorated ZnO-reduced graphene oxide nanocomposites. RSC Adv 5:8918–8928. https://doi.org/10.1039/C4RA13245A

27. Masudy-Panah S, Siavash Moakhar R, Chua CS et al (2017) Stable and efficient CuO based photocathode through oxygen-rich composition and Au–Pd nanostructure incorporation for solar-hydrogen production. ACS Appl Mater Interfaces 9:27596–27606. https://doi.org/10.1021/acsami.7b02685

28. Zolriasatein A, Shokuhfar A, Safari F, Abdi N (2017) Comparative study of SPEX and planetary milling methods for the fabrication of complex metallic alloy nanoparticles. Micro Nano Lett 13:448–451. https://doi.org/10.1049/mnl.2017.0608

29. Zolriasatein A, Shokuhfar A (2015) Size effect on the melting temperature depression of $Al_{12}Mg_{17}$ complex metallic alloy nanoparticles prepared by planetary ball milling. Phys E 74:101–107. https://doi.org/10.1016/j.physe.2015.06.015

30. Hou W, Dehm N, Scott RWJ (2008) Alcohol oxidations in aqueous solutions using Au, Pd, and bimetallic AuPd nanoparticle catalysts. J Catal 253:22–27. https://doi.org/10.1016/j.jcat.2007.10.025

31. Liu B, Aydil ES (2009) Growth of oriented single-crystalline rutile TiO_2 nanorods on transparent conducting substrates for dye-sensitized solar cells. J Am Chem Soc 131:3985–3990. https://doi.org/10.1021/ja8078972

32. Rutile phase, Joint Committee on Powder Diffraction Standards (JCPDC) card no 21-1276

33. Gold, Joint Committee on Powder Diffraction Standards (JCPDC) card no 04-0784

34. Palladium, Joint Committee on Powder Diffraction Standards (JCPDC) card no 01-1201

35. Kruse N, Chenakin S (2011) XPS characterization of Au/TiO_2 catalysts: binding energy assessment and irradiation effects. Appl Catal A 391:367–376. https://doi.org/10.1016/j.apcata.2010.05.039

36. Fang J, Cao SW, Wang Z et al (2012) Mesoporous plasmonic Au–TiO_2 nanocomposites for efficient visible-light-driven photocatalytic water reduction. Int J Hydrogen Energy 37:17853–17861. https://doi.org/10.1016/j.ijhydene.2012.09.023

37. Lay B, Sabri YM, Ippolito SJ, Bhargava SK (2014) Galvanically replaced Au–Pd nanostructures: study of their enhanced elemental mercury sorption capacity over gold. Phys Chem Chem Phys 16:19522–19529. https://doi.org/10.1039/c4cp02233e

38. Brun M, Berthet A, Bertolini J (1999) XPS, AES and Auger parameter of Pd and PdO. J Electron Spectrosc Relat Phenom 104:55–60. https://doi.org/10.1016/S0368-2048(98)00312-0

39. Liu Y, Juang L (2004) Electrochemical methods for the preparation of gold-coated TiO_2 nanoparticles with variable coverages. Langmuir 20:6951–6955

40. Wu Y, Liu H, Zhang J, Chen F (2009) Enhanced photocatalytic activity of nitrogen-doped titania by deposited with gold. J Phys Chem C 113:14689–14695. https://doi.org/10.1021/jp904465d

41. Zielińska-Jurek A, Kowalska E, Sobczak JW et al (2011) Preparation and characterization of monometallic (Au) and bimetallic (Ag/Au) modified-titania photocatalysts activated by visible light. Appl Catal B 101:504–514. https://doi.org/10.1016/j.apcatb.2010.10.022

42. Pal A, Shah S, Devi S (2007) Preparation of silver, gold and silver-gold bimetallic nanoparticles in w/o microemulsion containing TritonX-100. Colloids Surf A 302:483–487. https://doi.org/10.1016/j.colsurfa.2007.03.032

43. Ferrando R, Jellinek J, Johnston RL (2008) Nanoalloys: from theory to applications of alloy clusters and nanoparticles. Chem Rev 108:845–910. https://doi.org/10.1021/cr040090g

44. Maringa A, Mashazi P, Nyokong T (2015) Electrocatalytic activity of bimetallic Au-Pd nanoparticles in the presence of cobalt tetraaminophthalocyanine. J Colloid Interface Sci 440:151–161. https://doi.org/10.1016/j.jcis.2014.10.056

45. Parkinson B (1984) On the efficiency and stability of photoelectrochemical devices. Acc Chem Res 17:431–437. https://doi.org/10.1021/ar00108a004

46. Zielińska-Jurek A (2014) Progress, challenge, and perspective of bimetallic TiO_2-based photocatalysts. J Nanomater 2014:1–17. https://doi.org/10.1155/2014/208920

47. Mahshid S, Li C, Mahshid SS et al (2011) Sensitive determination of dopamine in the presence of uric acid and ascorbic acid using TiO_2 nanotubes modified with Pd, Pt and Au nanoparticles. Analyst 136:2322–2329. https://doi.org/10.1039/c1an15021a

48. Dimitratos N, Porta F, Prati L (2005) Au, Pd (mono and bimetallic) catalysts supported on graphite using the immobilisation method: synthesis and catalytic testing for liquid phase oxidation of glycerol. Appl Catal A 291:210–214. https://doi.org/10.1016/j.apcata.2005.01.044

49. Gomes Silva C, Juárez R, Marino T et al (2011) Influence of excitation wavelength (UV or visible light) on the photocatalytic activity of titania containing gold nanoparticles for the generation of hydrogen or oxygen from water. J Am Chem Soc 133:595–602. https://doi.org/10.1021/ja1086358

50. Balcha T, Strobl JR, Fowler C et al (2011) Selective aerobic oxidation of crotyl alcohol using aupd core-shell nanoparticles. ACS Catal 1:425–436. https://doi.org/10.1021/cs200040a

51. Dhara S, Giri PK (2011) On the origin of enhanced photoconduction and photoluminescence from Au and Ti nanoparticles decorated aligned ZnO nanowire heterostructures. J Appl Phys 110:124317. https://doi.org/10.1063/1.3671023

52. Wei C, Bee S, Basirun WJ (2014) Effect of Ce doping on RGO-TiO_2 nanocomposite for high photoelctrocatalytic behavior. Int J Photoenergy 2014:1–9. https://doi.org/10.1155/2014/141368

53. Dupuy L, Haller S, Rousset J et al (2010) Impedance measurements of nanoporosity in electrodeposited ZnO films for DSSC. Electrochem Commun 12:697–699. https://doi.org/10.1016/j.elecom.2010.03.009

54. Guo X, Diao P, Xu D et al (2014) CuO/Pd composite photocathodes for photoelectrochemical hydrogen evolution reaction. Int J Hydrogen Energy 39:7686–7696. https://doi.org/10.1016/j.ijhydene.2014.03.084

55. Parker RA (1961) Static dielectric constant for rutile (TiO_2), 1.6-1060 K. Phys Rev 124:1719–1722

56. Wang Y, Zhang YY, Tang J et al (2013) Simultaneous etching and doping of TiO_2 nanowire arrays for enhanced photoelectrochemical performance. ACS Nano 7:9375–9383. https://doi.org/10.1021/nn4040876

57. Hou W, Cronin SB (2013) A review of surface plasmon resonance-enhanced photocatalysis. Adv Funct Mater 23:1612–1619. https://doi.org/10.1002/adfm.201202148

58. Haro M, Abargues R, Herraiz-Cardona I et al (2014) Plasmonic versus catalytic effect of gold nanoparticles on mesoporous TiO2 electrodes for water splitting. Electrochim Acta 144:64–70. https://doi.org/10.1016/j.electacta.2014.07.146

Affiliations

Roozbeh Siavash Moakhar[1,2,3] · **Mahsa Jalali**[1,2] · **Ajay Kushwaha**[2] · **Gregory Kia Liang Goh**[2] · **Nastaran Riahi-Noori**[3] · **Abolghasem Dolati**[1] · **Mohammad Ghorbani**[1]

✉ Roozbeh Siavash Moakhar
roozbehsiavash@gmail.com

✉ Mohammad Ghorbani
ghorbani@sharif.edu

[1] Department of Materials Science and Engineering, Sharif University of Technology, Azadi Avenue, Tehran 11365-9466, Iran

[2] Institute of Materials Research and Engineering, Agency for Science, Technology and Research (A*STAR), 2 Fusionopolis Way, Innovis, #08-03, Singapore 138634, Singapore

[3] Non-Metallic Materials Research Group, Niroo Research Institute, Tehran, Iran